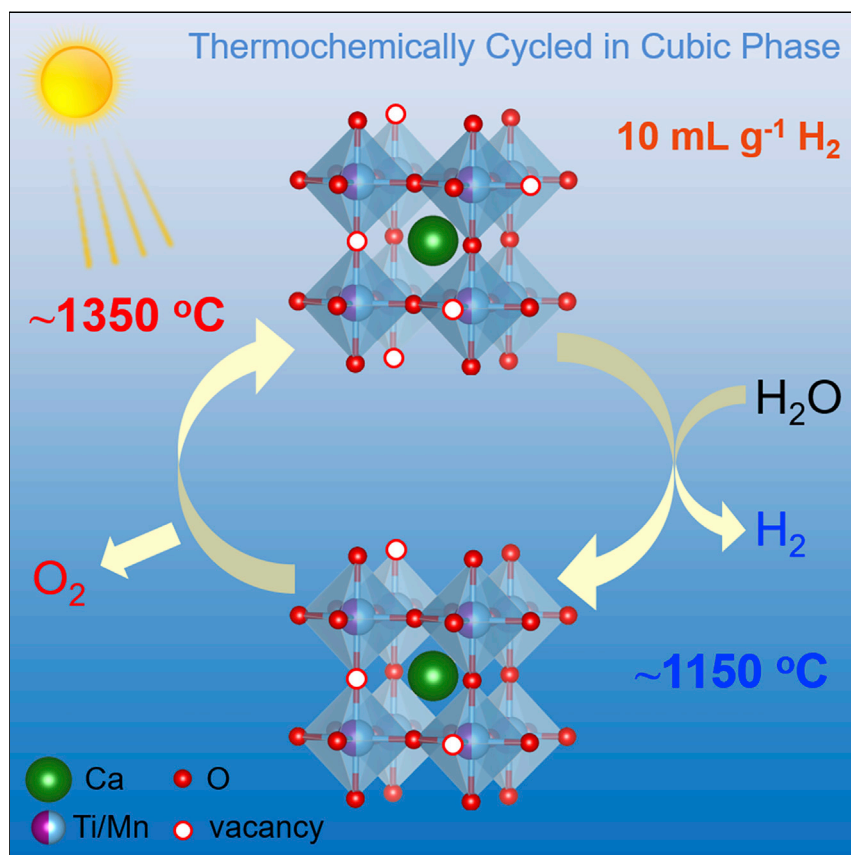


Article

Outstanding Properties and Performance of $\text{CaTi}_{0.5}\text{Mn}_{0.5}\text{O}_{3-\delta}$ for Solar-Driven Thermochemical Hydrogen Production

The combination of high thermal stability, rapid kinetics, moderate enthalpy of reduction, and large entropy of reduction in the perovskite $\text{CaTi}_{0.5}\text{Mn}_{0.5}\text{O}_{3-\delta}$ enables an outstanding thermochemical hydrogen productivity of 10.0 mL g^{-1} at a thermal reduction temperature of just $1,350^{\circ}\text{C}$ and a short cycle time of 1.5 h.

Xin Qian, Jianguang He,
Emanuela Mastronardo, Bianca
Baldassarri, Weizi Yuan,
Christopher Wolverton, Sossina
M. Haile

xinqian2021@u.northwestern.edu (X.Q.)
sossina.haile@northwestern.edu (S.M.H.)

HIGHLIGHTS

Large entropy of reduction and
intermediate enthalpy of
reduction

$p\text{O}_2$ -dependent reversible
structural transition:
orthorhombic \rightarrow tetragonal \rightarrow
cubic

Outstanding H_2 yield of 10 mL g^{-1}
upon reduction at $1,350^{\circ}\text{C}$ and a
cycle time 1.5 h

H_2 production rate limited by gas-
phase mass transport rather than
material kinetics



Understanding

Dependency and conditional studies
on material behavior

Qian et al., Matter 4, 1–21

February 3, 2021 © 2020 The Authors. Published
by Elsevier Inc.

<https://doi.org/10.1016/j.matt.2020.11.016>

Article

Outstanding Properties and Performance of $\text{CaTi}_{0.5}\text{Mn}_{0.5}\text{O}_{3-\delta}$ for Solar-Driven Thermochemical Hydrogen Production

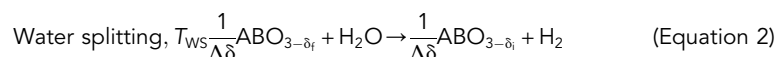
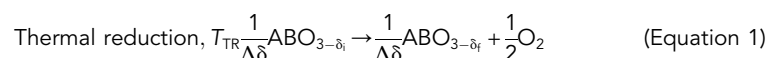
Xin Qian,^{1,*} Jiangang He,¹ Emanuela Mastronardo,^{1,4} Bianca Baldassarri,² Weizi Yuan,¹ Christopher Wolverton,^{1,2} and Sossina M. Haile^{1,2,3,5,*}

SUMMARY

Variable valence oxides of the perovskite crystal structure have emerged as promising candidates for solar hydrogen production via two-step thermochemical cycling. Here, we report the exceptional efficacy of the perovskite $\text{CaTi}_{0.5}\text{Mn}_{0.5}\text{O}_{3-\delta}$ (CTM55) for this process. The combination of intermediate enthalpy, ranging between 200 and 280 $\text{kJ}(\text{mol-O})^{-1}$, and large entropy, ranging between 120 and 180 $\text{J}(\text{mol-O})^{-1}\text{K}^{-1}$, of CTM55 create favorable conditions for water splitting. The oxidation state changes are dominated by Mn, with Ti stabilizing the cubic phase and increasing its reduction enthalpy. A hydrogen yield of $10.0 \pm 0.2\text{ mL g}^{-1}$ is achieved in a cycle between $1,350^\circ\text{C}$ (reduction) and $1,150^\circ\text{C}$ (water splitting) and a total cycle time of 1.5 h, exceeding all previous fuel production reports. The gas evolution rate suggests rapid material kinetics, and, at $1,150^\circ\text{C}$ and higher, a process primarily limited by the magnitude of the thermodynamic driving force.

INTRODUCTION

A global transition away from fossil fuel energy to sustainable sources, in particular solar energy, requires breakthroughs in energy storage.^{1,2} Two-step solar thermochemical hydrogen (STCH) production has emerged as an attractive route for meeting this demand.^{3,4} Key features of this approach include utilization of the entire solar spectrum, operation in the absence of precious metal catalysts, and temporal differentiation between hydrogen and oxygen production steps, simplifying gas separation. The two-step cycling approach is readily implemented using non-stoichiometric oxides because such materials can retain their structural integrity throughout the cycling process.⁵ The two half-cycles are (1) high-temperature thermal reduction carried out at temperature T_{TR} , Equation 1, in which the oxide releases a portion of the oxygen in its structure to the gas phase, and (2) usually at lower temperature, oxidation of the structure by steam at temperature T_{WS} , Equation 2, in which the water is “split” and hydrogen is released.



Here, δ_i and δ_f are the oxygen non-stoichiometry values at the initiation and completion, respectively, of the reduction half-cycle, and $\Delta\delta = \delta_f - \delta_i$ is the change in non-stoichiometry through the cycling process.

Progress and Potential

A global transition away from fossil fuel energy to sustainable sources, in particular solar energy, requires breakthroughs in energy storage. Two-step solar thermochemical hydrogen (STCH) production, which utilizes the entire solar spectrum, functions in the absence of precious metal catalysis, and yields hydrogen and oxygen separately, has emerged as an attractive route for meeting this demand. Here, we report the thermochemical properties of $\text{CaTi}_{0.5}\text{Mn}_{0.5}\text{O}_{3-\delta}$. The combination of large entropy and moderate enthalpy of reduction, along with rapid material kinetics, results in an outstanding hydrogen productivity of 10 mL g^{-1} with reduction temperature at just $1,350^\circ\text{C}$ and a short cycle time of 1.5 h. The material furthermore displays excellent thermal stability. Beyond performance metrics, the thermodynamic data connect material chemistry to hydrogen yields for arbitrary cycling conditions, a critical step toward designing materials suitable for widespread commercial adoption.

To date, two major classes of non-stoichiometric oxides have been evaluated for STCH applications, fluorites and perovskites. The fluorites are largely constrained to ceria and its derivatives,^{5,6} whereas the perovskites,^{7,8} explicitly represented in Equations 1 and 2, offer an enormous range of possible chemistries. Ceria-based materials require excessively high temperatures, ideally $>1,500^\circ\text{C}$, to generate non-negligible quantities of hydrogen through the cycling process, and chemical modifications have produced only moderate gains toward the goal or reduced temperature operation.⁶ Thus, attention has increasingly turned toward the perovskites, with the goal of identifying materials that display suitable thermodynamic characteristic, i.e., enthalpy and entropy of reduction, so as to drive both steps of the STCH process at accessible temperatures. Two-temperature, two-step thermochemical cycling benefits monotonically with increases in the entropy of oxidation, whereas an intermediate value of the enthalpy of oxidation is required, depending on the cycling conditions.⁹ Recent computational surveys have suggested that perovskites with Mn^{4+} on the B-site will display suitable enthalpies.^{8,10} Experimental studies have validated these predictions and furthermore indicate that such materials will have sufficiently high entropies.¹⁰

Driven by these considerations, we examine here $\text{Ca}(\text{Ti}_{0.5}\text{Mn}_{0.5})\text{O}_3$ (CTM55), a compound which not only stands to meet the thermodynamic requirements for STCH applications due to the incorporation of Mn^{4+} , but also benefits from a composition formed entirely of earth-abundant elements. The end-member CaMnO_3 has been evaluated as a potential oxygen storage material.^{11,12} At ambient conditions it adopts a distorted orthorhombic perovskite structure (the GdFeO_3 structure type), undergoing successive transitions to tetragonal then cubic phases on heating and loss of oxygen.^{12,13} Introduction of redox inactive elements on the B-site of transition metal perovskites has recently proven to be a highly effective tool for tuning their thermodynamic properties. In particular, introduction of Al into $(\text{La},\text{Sr})\text{MnO}_3$ ^{14,15} and introduction of 10% Fe into CaMnO_3 ¹² (where both Al and Fe are strictly 3+) have been shown to modify the enthalpy while largely retaining the surprising high entropy that is characteristic of CaMnO_3 . Distinct from Al and Fe, the Ti dopant of this work can be expected to remain in the 4+ oxidation state during redox cycling. In such a case, the configurational entropy associated with the reduction reaction might be expected to scale with $-\ln\left(\frac{\delta}{3-\delta}\right)$, as opposed to the smaller term $-\ln\left(\frac{\delta}{3-0.5x-\delta}\right)$, where x is the 3+ dopant concentration and the argument in the ln is the number of ways of arranging oxygen vacancies in the structure, motivating consideration of the tetravalent species. Furthermore, similar to CaMnO_3 , CTM55 adopts a distorted orthorhombic perovskite structure,¹⁶ and can be anticipated to transform to a cubic phase on heating. Depending on the phase boundaries between the orthorhombic and presumed tetragonal and cubic phases, moderate step changes in oxygen content, which have the potential of enhancing fuel productivity, may be expected at such transitions.

In this work, we present a comprehensive study of the structural evolution, redox thermodynamics, and thermochemical water-splitting capacity of CTM55. The structural evolution is tracked by *in situ* high-temperature X-ray diffraction (XRD) measurements, complemented by *in situ* high-temperature X-ray absorption near edge spectroscopy (XANES) of thin-film CTM55, providing insight into the relative redox activity of the Mn and Ti species. Thermodynamic properties are evaluated using simultaneous differential scanning calorimetry (DSC) and thermogravimetric analysis (TGA) to detect phase transitions and obtain mass as a function of oxygen partial pressure ($p\text{O}_2$) and temperature. From these data, the enthalpy and entropy of reduction are determined as functions of δ . Although a detailed chemical model

¹Department of Materials Science and Engineering, Northwestern University, Evanston, IL 60208, USA

²Program of Applied Physics, Northwestern University, Evanston, IL 60208, USA

³Department of Chemistry, Northwestern University, Evanston, IL 60208, USA

⁴Institute of Catalysis and Petrochemistry, Spanish National Research Council (CSIC), C/ Marie Curie, 2, Madrid 28049, Spain

⁵Lead Contact

*Correspondence:
xingqian2021@u.northwestern.edu (X.Q.),
sossina.haile@northwestern.edu (S.M.H.)
<https://doi.org/10.1016/j.matt.2020.11.016>

has not been developed from these properties, the values were found to be particularly well suited for STCH applications. Thermochemical water-splitting experiments are performed to directly assess the hydrogen production efficacy. The gas evolution profiles are compared with computed profiles expected for the case in which the material remains in quasi-equilibrium with the gas phase throughout the cycling (i.e., is gas-phase mass transport limited), providing insight into the relative roles of material kinetic and thermodynamic limitations to the macroscopic rate of fuel production. Overall, the combination of high thermal stability, favorable thermodynamics, and fast kinetics found in CTM55 render it a competitive material for high-capacity thermochemical hydrogen production.

RESULTS AND DISCUSSION

Synthesis, Phase Transition, and Stability

Starting powders of CTM55 were prepared by solid-state methods involving a final reaction step at 1,400°C in air, upon completion of which the sample was furnace cooled to room temperature. Rietveld analysis of the XRD pattern of the resulting material (Figure S1A) revealed a perovskite structure of the GdFeO_3 type with an orthorhombic distortion and a random arrangement of Ti and Mn on the B-site. The refined lattice constants are $a = 5.3603(1)$, $b = 7.5506(2)$, $c = 5.3262(1)$ Å. Porous self-supporting monoliths (~50% porosity) were prepared for TGA and thermochemical water-splitting measurements (Figure S1B). The open structure ensures easy gas access to the entire mass of sample, high surface area for the surface reaction step, and short bulk diffusion lengths for oxygen migration. For pulsed laser deposition (PLD) of thin films, a dense target (~97% relative density) was fabricated by uniaxial and isostatic pressing of ball-milled CTM55 fine powder and sintering at 1,400°C (Figure S1C). Elemental analysis by X-ray energy dispersive spectroscopy (EDS) collected at multiple positions on the polished dense surface yielded the cation ratio of Ca:Ti:Mn to be $50.03 \pm 0.05 : 25.09 \pm 0.04 : 24.88 \pm 0.10$ (Figure S1D). Similarly, quantitative chemical analysis by inductively coupled plasma-optical emission spectrometry (ICP-OES) revealed a Ca:Ti:Mn molar ratio of $50.00 \pm 0.01 : 25.15 \pm 0.02 : 25.35 \pm 0.02$. Both measurements revealed that the targeted stoichiometry had been attained. Further cross-validation of the stoichiometry was derived from a complete reduction experiment for the measurement of reference state oxygen content, as described below.

Simultaneous thermogravimetry and differential scanning calorimetry (TG-DSC) measurements were carried out under three $p\text{O}_2$ conditions (0.208, 0.028, and 4.20×10^{-5} atm) using a relatively fast ramp rate of $10^\circ\text{C min}^{-1}$ so as to detect phase transitions (Figure 1). The DSC data under the two higher $p\text{O}_2$ conditions (Figure 1B) reveal two reversible phase transitions, which correspond to structural changes from the orthorhombic to a tetragonal phase and then to a cubic phase, with a narrow 30°C – 40°C window of stability for the tetragonal phase. The transitions shift toward lower temperatures with decreasing $p\text{O}_2$. At the lowest $p\text{O}_2$ condition, only a single, irreversible thermal event is detected, suggesting a direct transition from the orthorhombic to the cubic phase, which is then retained on cooling. Mass loss in all three measurements (Figure 1A) occurs predominantly, but not entirely, from the high-temperature cubic phase. In the two higher $p\text{O}_2$ measurements, despite the 10°C – 20°C hysteresis in the structural transitions as measured by DSC, the mass profiles on heating and cooling are almost entirely coincident with one another, and the system $p\text{O}_2$ is invariant (Figure 1C), indicating equilibrium to near equilibrium oxygen loss and uptake. The mass equilibration is further evident from the invariance in the sample weight during the isothermal hold at 1,200°C (Figure 1D), which

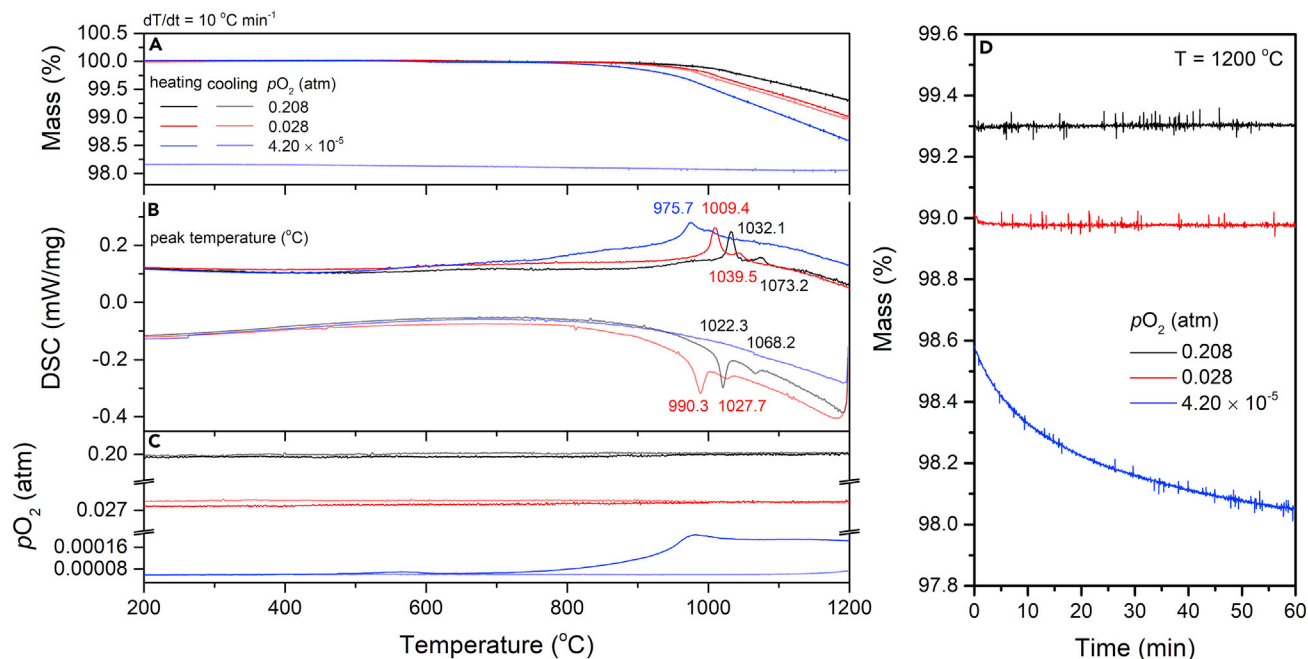


Figure 1. Thermal Properties of CTM55

Simultaneous thermogravimetry and differential scanning calorimetry (TG-DSC) measurement of CTM55 during both heating and cooling for three different inlet $p\text{O}_2$ values, as indicated: (A) mass profiles; (B) DSC profiles; (C) $p\text{O}_2$ profiles; and (D) mass profiles during isothermal hold. Experiments performed using capped Pt crucibles, temperature ramp rate of $10^\circ\text{C min}^{-1}$, and a cylindrical porous sample, 174.68 mg in mass.

sharply contrasts that for the low $p\text{O}_2$ measurement. Overall, the behavior of CTM55 is exactly analogous to what has been found in CaMnO_3 ,¹² which similarly undergoes orthorhombic to tetragonal to cubic transitions on heating that shift to lower temperatures with decreasing $p\text{O}_2$, with very low $p\text{O}_2$ conditions producing a direct orthorhombic to cubic transition. The transition temperatures measured here for CTM55 are summarized in Table S1. It is to be noted that typical thermochemical cycling conditions for hydrogen production, which expose a material to an effective $p\text{O}_2$ of no more than $\sim 1.2 \times 10^{-6}$ atm at 800°C and $\sim 4.8 \times 10^{-6}$ atm at $1,000^\circ\text{C}$, would leave CTM55 within the stability regime of the cubic phase throughout the cycling process. More oxidizing conditions in the water-splitting half-cycle would be required to take advantage of the step-change in oxygen stoichiometry of the material at the crystallographic phase transitions.

High-temperature *in situ* XRD patterns were collected under ambient air in 100°C steps between 600°C and $1,400^\circ\text{C}$, on both heating and cooling (ramp rate $10^\circ\text{C min}^{-1}$). The results (Figure 2) directly revealed the reversible transition between orthorhombic and cubic phases, with the cubic phase accounting for all of the diffraction peaks at $1,200^\circ\text{C}$ and higher. Representative Rietveld refinement results are presented in Figure S2. No attempt was made to capture the tetragonal phase in these experiments due to the narrow temperature range over which this phase exists. The refined lattice constants are well behaved, showing expansion on heating, presumably due to a combination of thermal and chemical expansion (Figure S3), and a slight increase in slope at the transition to the cubic phase. These thermal analyses and *in situ* diffraction experiments reveal that CTM55 is thermally stable to at least $1,400^\circ\text{C}$. *Ex situ* diffraction studies of the material after exposure to higher temperatures for thermal analysis and thermogravimetric studies (Table S2) revealed minimum stability conditions of $1,600^\circ\text{C}$ under air and $1,450^\circ\text{C}$ under $p\text{O}_2 = 4.20 \times 10^{-5}$ atm (Figure S4).

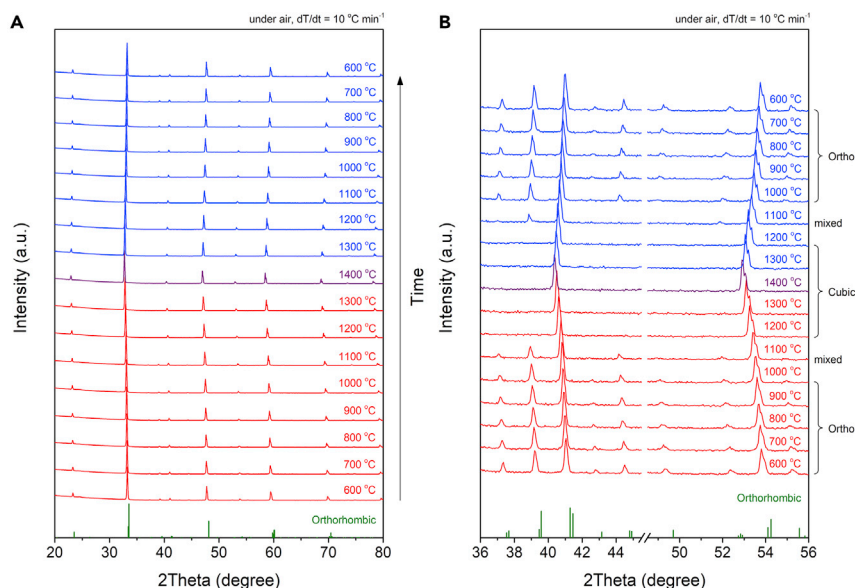


Figure 2. Crystallographic Properties of CTM55

High-temperature *in situ* XRD of CTM55 under air at a heating and cooling rate of $10^\circ\text{C min}^{-1}$, with data obtained at the temperatures indicated: (A) upon heating and cooling in the temperature range from 600°C to $1,400^\circ\text{C}$; (B) enlarged diffraction patterns in selected 2θ ranges.

Thermodynamics of Reduction

Before the measurement of the mass of CTM55 over a range of temperatures and $p\text{O}_2$ values, the oxygen content at a specified reference condition, selected here as $T = 1,000^\circ\text{C}$, $p\text{O}_2 = 0.075$ atm, was determined by TGA via a complete reduction experiment (Figure S5A). The experiment was also used to corroborate the material composition. In brief, *ex situ* XRD analysis of the reduction products revealed stoichiometric phases of CaTiO_3 and $\text{Ca}_{0.5}\text{Mn}_{0.5}\text{O}$ (Figure S5B), implying that all of the Mn was completely reduced to the 2+ oxidation state, whereas the Ti retained the 4+ oxidation state even under extremely reducing conditions. The phase fractions of the reduction products implied a Ca:Ti:Mn molar ratio of $50.0 \pm 0.5 : 25.2 \pm 0.1 : 24.8 \pm 0.2$. Evaluation of the total mass loss was also consistent with the quantity of Mn in the material.

Thermogravimetric analyses were carried out up to a maximal temperature of $1,500^\circ\text{C}$ under ten different $p\text{O}_2$ conditions in the range of $0.208\text{--}4.20 \times 10^{-5}$ atm (Table S3), with a measurement of the mass at the reference state included in each suite of experiments. A challenge with TGA measurements of oxygen non-stoichiometry arises from the competing needs to (1) sweep out the oxygen evolved from the sample quickly enough that the sample environment does not change during the experiment, a situation that is exacerbated when the measurement is carried out under low $p\text{O}_2$ and hence relative mass changes are large, and (2) attain sufficiently high sensitivity when relative mass changes are small, a situation exacerbated when the measurement is carried out under moderate to high $p\text{O}_2$ and, additionally, the absolute sample mass is small. Experiments performed here were designed to address these challenges. Specifically, measurements under $p\text{O}_2$ values of 2.14×10^{-4} atm and higher were performed using a large sample (1.604 g), whereas those under lower $p\text{O}_2$ were performed using a smaller sample (0.945 g). Furthermore, for measurements under $p\text{O}_2$ conditions of 0.028 atm and higher, the mass loss profiles a slow ramp of 2°C min^{-1} , which was utilized, and data recorded during both heating

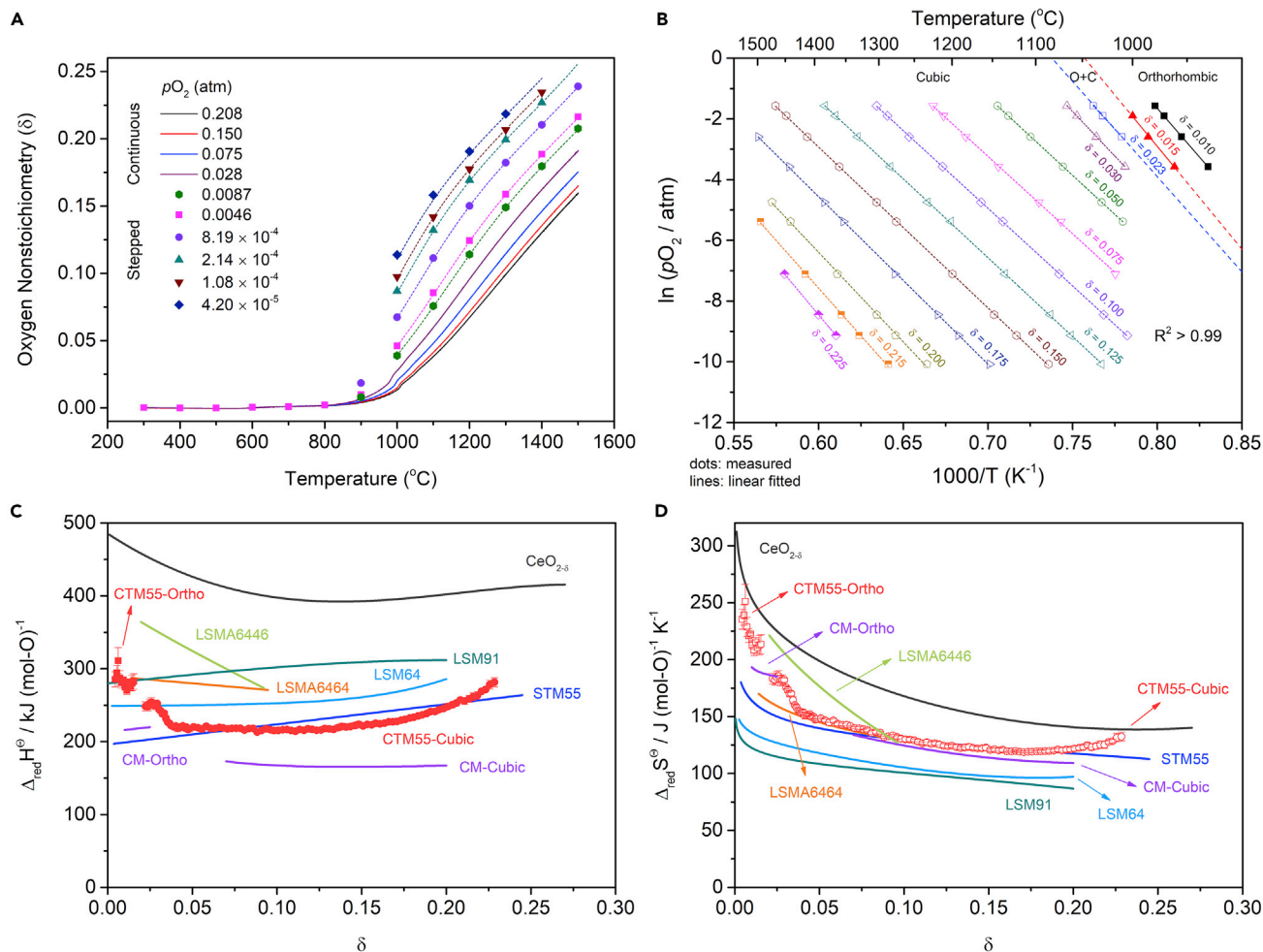


Figure 3. Oxygen Non-stoichiometry and Thermodynamic Properties of CTM55 Perovskite

(A) oxygen non-stoichiometry as measured from both continuous and stepwise heating at the $p\text{O}_2$ values indicated; (B) Arrhenius presentation for extraction of thermodynamic properties by the van't Hoff method at representative fixed δ between 0.010 and 0.225; (C) standard enthalpy of reduction; and (D) standard entropy of reduction. In (C) and (D) results obtained in this work for CTM55 are presented alongside literature data for $\text{La}_{0.6}\text{Sr}_{0.4}\text{Mn}_{0.4}\text{Al}_{0.6}\text{O}_{3-\delta}$ (LSMA6446),¹⁵ $\text{La}_{0.6}\text{Sr}_{0.4}\text{Mn}_{0.6}\text{Al}_{0.4}\text{O}_{3-\delta}$ (LSMA6464),¹⁵ $\text{La}_{0.9}\text{Sr}_{0.1}\text{MnO}_{3-\delta}$ (LSM91),¹⁷ $\text{La}_{0.6}\text{Sr}_{0.4}\text{MnO}_{3-\delta}$ (LSM64),¹⁷ $\text{SrTi}_{0.5}\text{Mn}_{0.5}\text{O}_{3-\delta}$ (STM55),¹² $\text{CaMnO}_{3-\delta}$ (CM),¹² and $\text{CeO}_{2-\delta}$.¹⁹ In (A) solid lines and symbols are measured values, whereas dashed lines are calculated using fitted $\Delta_{\text{red}}H^{\ominus}(\delta)$ and $\Delta_{\text{red}}S^{\ominus}(\delta)$ functions (see Figure S12, Supplemental Information).

and cooling. Agreement between the two profiles and invariance of the measured $p\text{O}_2$ (Figure S6) were used to confirm that equilibrium values had been obtained. For measurements under $p\text{O}_2$ conditions of 0.0087 atm and lower, a stepped heating protocol involving 100°C steps with 1–5 h hold times was used (Figure S7) and equilibrium assured in most cases by return of the measured $p\text{O}_2$ to the inlet value. Under the most reducing conditions, the equilibrium mass was determined by extrapolation (Figures S8 and S9).

Shown in Figure 3A are the oxygen non-stoichiometry profiles implied by the TGA, with solid lines and discrete points derived from continuous and stepped measurements, respectively. Dashed lines are fits calculated from the thermodynamics properties of CTM55 described below. Evident in the continuous profiles is a small anomaly at a temperature of $\sim 980^{\circ}\text{C}$. This feature reflects the transition to the cubic phase, behavior also observed in $\text{CaMnO}_{3-\delta}$.¹² Transition temperatures obtained

from the derivative of the mass loss profiles are in good agreement with the DSC results (Table S1), and again show the shift toward lower temperature with decreasing $p\text{O}_2$.

The mass loss behavior reflects the thermodynamics of the reduction reaction expressed in Equation 1 and provides a means of quantifying the associated thermodynamic functions. In the limit of infinitesimal extent of reduction ($\Delta\delta \rightarrow 0$), the Gibbs energy of reduction at specified δ also tends to zero ($\Delta_{\text{red}}G(T, \delta) \rightarrow 0$). Thus, the equilibrium reaction constant, $K_{\text{red}}^{\text{eq}}$, is given by

$$K_{\text{red}}^{\text{eq}} = (\hat{p}\text{O}_2)^{1/2} = \exp\left\{\frac{-\Delta_{\text{red}}G^\ominus(T, \delta)}{RT}\right\} = \exp\left\{\frac{-\Delta_{\text{red}}H^\ominus(\delta) + T\Delta_{\text{red}}S^\ominus(\delta)}{RT}\right\} \quad (\text{Equation 3})$$

in which the term $\hat{p}\text{O}_2$ is $p\text{O}_2/p_{\text{ref}}$, equal to the $p\text{O}_2$ referenced to the standard pressure, $p_{\text{ref}} = 1$ atm. R is the universal gas constant, T is the temperature, $\Delta_{\text{red}}G^\ominus(T, \delta)$, $\Delta_{\text{red}}H^\ominus(\delta)$, and $\Delta_{\text{red}}S^\ominus(\delta)$ are the standard Gibbs energy, standard enthalpy, and standard entropy of reduction at specified δ , respectively, per mole of oxygen. Rearranging Equation 3, yields

$$R\ln(\hat{p}\text{O}_2)^{1/2} = -\frac{\Delta_{\text{red}}H^\ominus(\delta)}{T} + \Delta_{\text{red}}S^\ominus(\delta) \quad (\text{Equation 4})$$

While $\Delta_{\text{red}}S^\ominus(\delta)$ is strongly dependent on non-stoichiometry because it includes the configurational entropy of the defect-laden oxide, $\Delta_{\text{red}}H^\ominus(\delta)$ may be only weakly dependent on δ . Both terms typically have negligible dependence on temperature. Following the van't Hoff method,²⁰ an Arrhenius plot of T - $p\text{O}_2$ pairs at each δ was prepared, and the enthalpy and entropy of reduction extracted from the slopes and intercepts, respectively. Representative datasets at selected δ are displayed in Figure 3B.

The enthalpy and entropy values obtained from this analysis are presented in Figures 3C and 3D, respectively. Fit functions describing these thermodynamic terms are provided in Figure S12. The small range of δ over which the orthorhombic phase exists ($\delta < 0.015$) implies a relatively high uncertainty for the properties of this phase. For similar reasons, the uncertainty is high in the thermodynamic properties of the cubic phase in the small δ region (0.023–0.038). Nevertheless, the results reveal that both the enthalpy and the entropy of orthorhombic CTM55 are larger than the respective values in the cubic phase. In terms of high-temperature cycling, the relevant behavior is captured in the high δ region, within which the experimental uncertainty is relatively small (and the material remains in the cubic phase). An interesting feature of the raw non-stoichiometry behavior of CTM55 (Figure 3A) is the apparent onset of a plateau at $\delta = 0.25$, reflected in turn in upward trends in both the entropy and enthalpy at this δ . Presuming the Ti remains fully oxidized, this non-stoichiometry coincides with a mean Mn oxidation state of 3+. Anomalies in the thermodynamic properties of variable valence oxides are known to occur at transitions in electronic behavior (e.g., from n-type to p-type),^{21–23} and such a transition may explain the observations here. From the perspective of thermochemical cycling, so long as significant extrapolations are avoided, the equilibrium hydrogen production capacity for any given set of cycling conditions can be computed from the fully determined thermodynamic properties. Representative calculations are presented in Figure S13.

To put the properties of CTM55 in context, the thermodynamic data for several additional materials, specifically, $\text{SrTi}_{0.5}\text{Mn}_{0.5}\text{O}_{3-\delta}$ (STM55),¹⁸ $\text{CaMnO}_{3-\delta}$ (CM),¹² $\text{La}_{0.9}\text{Sr}_{0.1}\text{MnO}_{3-\delta}$ (LSM91),¹⁷ $\text{La}_{0.6}\text{Sr}_{0.4}\text{MnO}_{3-\delta}$ (LSM64),¹⁷ $\text{La}_{0.6}\text{Sr}_{0.4}\text{Mn}_{0.4}\text{Al}_{0.6}\text{O}_{3-\delta}$

(LSMA6446),¹⁵ $\text{La}_{0.6}\text{Sr}_{0.4}\text{Mn}_{0.6}\text{Al}_{0.4}\text{O}_{3-\delta}$ (LSMA6464),¹⁵ and $\text{CeO}_{2-\delta}$,¹⁹ are included in Figures 3C and 3D. Higher entropy and enthalpy in the orthorhombic phase compared with the cubic phase is evident in CM,¹² similar to what is found here for CTM55. In $\text{CaMn}_{0.9}\text{Fe}_{0.1}\text{O}_{2.95-\delta}$ (CMF91)¹² (not shown) this trend is retained in the entropy, but not in the enthalpy. The comparisons further reveal that orthorhombic CTM55 displays a very high entropy, approaching that of $\text{CeO}_{2-\delta}$ and similar to that of LSMA6446, while the enthalpy is moderate, comparable with that of LSMA6464 and of LSM91. While this is an extremely attractive combination, cycling is in fact expected to occur with the material entirely within the cubic phase, as noted above. Within the cubic region, the thermodynamic properties of CTM55 are similar to those of STM55. The entropy remains high over a relatively wide δ range, and the enthalpy is somewhat lower than those of the $\text{La}_{1-x}\text{Sr}_x\text{MnO}_{3-\delta}$ and $\text{La}_{1-x}\text{Sr}_x\text{Mn}_y\text{Al}_{1-y}\text{O}_{3-\delta}$ series. Low enthalpy of reduction appears to be a feature of cubic or near-cubic perovskites in which the Mn oxidation state at ambient conditions is 4+, as suggested from computational studies.^{8,10} The introduction of Ti into CaMnO_3 has the desirable effect of increasing the enthalpy, with little impact on the entropy. The origins of the high entropy in CaMnO_3 and the B-site-doped derivatives are unclear, nor can it be concluded whether co-doping on the A- and B-sites ($\text{La}_{1-x}\text{Sr}_x\text{Mn}_y\text{Al}_{1-y}\text{O}_{3-\delta}$) yields distinctive behavior from B-site doping alone. The overall similarity of CTM55 and STM55 is somewhat surprising given the reported differences between the cubic forms of the end-members $\text{CaMnO}_{3-\delta}$ and $\text{SrMnO}_{3-\delta}$,¹³ but the enthalpy behavior generally agrees with recent computational predictions.⁸ The experimentally measured thermodynamic similarities suggest fuel production from CTM55 and STM55 will be similar, with any difference originating from differences in kinetic properties or material architecture.

In situ high-temperature XANES measurements were pursued in an attempt to reveal the relative contributions of the Mn and Ti species to the reduction behavior. While the complete reduction experiment by TGA showed CaTiO_3 as a final product, possible partial reduction of Ti at high temperature cannot be ruled out on the basis of this measurement alone. XANES experiments were performed using thin-film samples, ~200 nm in thickness, grown on sapphire substrates by PLD, using an experimental configuration shown elsewhere to be effective for probing the bulk oxidation state of variable valence oxides.²⁴ The as-prepared film was polycrystalline in nature, with the expected orthorhombic structure, and the material was found to be compatible with the sapphire substrate up to a temperature of 1,000°C (Figure S10). Spectra were collected at the Ti K edge and the Mn K edge in fluorescence mode, using the facilities at Sector 5 (5BM-D) of the Advanced Photon Source at Argonne National Laboratory (experimental details in Supplemental Information). Measurements were made under synthetic air at 800°C, 900°C, and 1,000°C, at which the oxygen non-stoichiometry values are small, but nonetheless finite: 0.0017, 0.0040, and 0.0134, respectively. Reflecting the limited changes in overall reduction extent, the XANES spectra for both elements were relatively unchanged upon heating from 800°C to 1,000°C (Figure S11). Close examination of the features of the Mn spectra, however, showed a slight shift of the edge energy toward lower values, from 6,554.76 to 6,554.34 eV, consistent with slight reduction of this element. In contrast, the Ti edge remained within 20 meV of 4,980.75 eV for all temperatures. Thus, Mn, rather than Ti, is indeed the redox active element, even at high temperature. The result presents an intriguing example of a valence-invariant element having a strong influence on the redox behavior of a material into which it is incorporated. The behavior is reminiscent of the influence of Zr on the properties of CeO_2 ,²⁰ and is consistent with the observation that the strictly trivalent dopant Al can have a profound influence on the thermodynamic properties of LSM materials.^{14,15}

Table 1. Measurement Conditions and Results of Thermochemical Cycling Experiments Performed Using CTM55

Figure & Cycle ID (M = Multi-Cycle)	Mass (g)	V_{TR} (mL min^{-1})	T_{WS} ($^{\circ}\text{C}$)	Average H_2 ($\text{mL min}^{-1} \text{g}^{-1}$)	Peak H_2 ($\text{mL min}^{-1} \text{g}^{-1}$)	Cumulative H_2 (mL g^{-1})	Equilibrium H_2 (mL g^{-1})
S14 M1	0.5215	500	900	0.084(6)	0.21(1)	5.1(1)	21.7
S15 M2	0.5215	500	1,000	0.101(4)	0.25(1)	6.0(1)	16.6
S16 M3	0.5215	500	1,100	0.110(6)	0.28(1)	6.6(1)	12.5
4(a) M4	0.5215	500	1,150	0.114(4)	0.30(1)	6.8(1)	10.7
S17 M5	0.5215	500	1,200	0.107(5)	0.30(1)	6.4(1)	9.1
S18 M6	0.5215	1,000	1,150	0.126(3)	0.37(1)	7.6(1)	10.7
4(b) M7	0.2559	1,000	1,150	0.166(8)	0.73(2)	10.0(2)	10.7

Computed equilibrium hydrogen productivity under each condition is also reported. Reduction was carried out under 10 ppm O_2 in Ar ($p_{\text{O}_2} = 10^{-5}$ atm) at $1,350^{\circ}\text{C}$ for 0.5 h at the reduction gas flow rate (V_{TR}) indicated, and oxidation (water splitting) was carried out under a flow rate of 300 mL min^{-1} of Ar with $p_{\text{H}_2\text{O}} = 0.4$ atm for 1 h at the water-splitting temperature (T_{WS}) indicated. A porous monolithic sample of mass indicated was used.

Thermochemical Water Splitting

Hydrogen production over CTM55 was measured in an in-house constructed thermochemical cycling station (experimental details in [Supplemental Information](#)). In most of the experiments, the material was cycled multiple times between fixed thermal reduction and fixed water-splitting conditions. These reactor-relevant experiments were used to identify conditions that yield high values of hydrogen productivity and to assess fuel production stability. Additional experiments were then performed in which oxygen evolution from a fully oxidized state was tracked, and subsequent fuel production for single half-cycles recorded. This experimental protocol was used for comparing gas evolution profiles with those expected for quasi-equilibrium behavior, as described below.

In all cases (for both classes of experiments), reduction was carried out at $1,350^{\circ}\text{C}$ under 10 ppm O_2 (balance Ar) and the steam partial pressure in the water-splitting step was 0.4 atm. If the reactions were permitted to proceed to equilibrium, extremely high values of hydrogen production would be expected for these conditions ([Figure S13](#)). For example, for water splitting at $1,000^{\circ}\text{C}$, an equilibrium hydrogen productivity of 16.6 mL g^{-1} is anticipated. To date, the highest STCH productivity reported for these conditions is 6.9 mL g^{-1} , obtained using the state-of-the-art perovskite $\text{La}_{0.6}\text{Sr}_{0.4}\text{Mn}_{0.6}\text{Al}_{0.4}\text{O}_{3-\delta}$ (LSMA6464).²⁵ Because of the diminishing rate of fuel production with time, it is implausible that thermochemical cycling would be performed in such a way as to achieve equilibrium fuel productivity. Nevertheless, this very high equilibrium value suggests that competitive hydrogen productivity will be obtained from CTM55 under reactor-relevant, fixed-length cycles with moderate cycle times.

Multiple Cycles Repeated Hydrogen Production

As summarized in [Table 1](#), a series of seven different cycling conditions were examined in the multi-cycle (denoted as M) experiments. All relevant parameters, specifically, sample mass, reactant gas volumetric flow rates (V_{TR} and V_{WS}), temperatures (T_{TR} and T_{WS}), gas compositions ($p_{\text{O}_2}^{\text{TR}}$ and $p_{\text{H}_2\text{O}}^{\text{WS}}$), and reaction times (t_{TR} and t_{WS}) are fully documented in [Table 1](#). In all cases, the heating from T_{WS} to T_{TR} was carried out under $p_{\text{O}_2}^{\text{TR}}$, whereas the $p_{\text{H}_2\text{O}}^{\text{WS}}$ was introduced after the quenching from T_{TR} to T_{WS} , as soon as the thermocouple registered that the desired temperature had been reached. For each set of conditions, 14 cycles were performed. In the first five cycling experiments, the reduction conditions were identical ($T_{\text{TR}} = 1,350^{\circ}\text{C}$, $p_{\text{O}_2}^{\text{TR}} = 10^{-5}$ atm, $t_{\text{TR}} = 0.5$ h), and only changes in the water-splitting step were

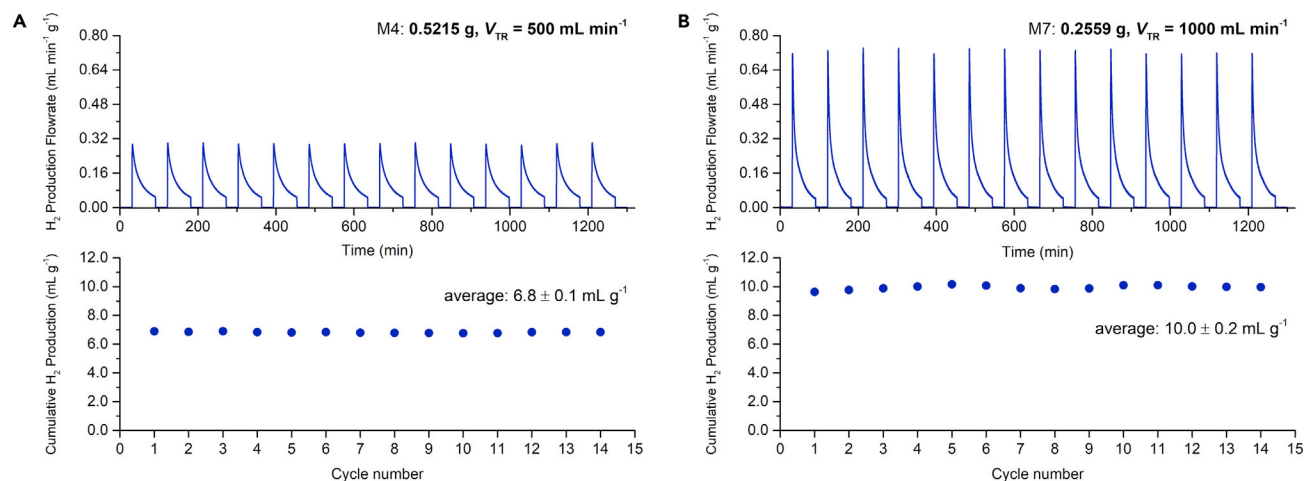


Figure 4. Cyclic Hydrogen Production over Porous Monolithic CTM55

(A) Hydrogen production using a relatively large mass and low gas flow rate in the reduction step; and (B) hydrogen production using a relatively small mass and high gas flow rate in the reduction step; with all other parameters held identical. Upper figures show instantaneous hydrogen production flow rates and lower figures show cumulative values for each cycle. Full details of the experimental conditions are given in Table 1.

examined. In the sixth and seventh cycling experiments, the impact of changing sample mass and reduction gas flow rate were explored. Sample mass and gas flow rate will influence the hydrogen production profile if the material is in quasi-equilibrium with the gas phase. Under such conditions, the material immediately equilibrates with the supplied gas and can react no further until the next infinitesimal unit of gas enters the reaction zone. Accordingly, the macroscopic rate will be a direction function of the mass normalized gas flow rate, as discussed further in the context of the single-cycle experiments. Here, the discussion begins with the impact of the mass and gas flow parameters on the multi-cycle experiments.

Shown in Figure 4 are two representative sets of cycling results obtained under superficially identical conditions (nominal): $T_{\text{TR}} = 1,350^\circ\text{C}$, $p\text{O}_2^{\text{TR}} = 10^{-5}$ atm, $t_{\text{TR}} = 0.5$ h, $T_{\text{WS}} = 1,150^\circ\text{C}$, $p\text{H}_2\text{O}^{\text{WS}} = 0.4$ atm, and $t_{\text{WS}} = 1$ h (M4 and M7, Table 1). The cycle-to-cycle reproducibility is high within each set of experiments, as was observed for all seven sets of cycling studies (Figures S14–S18). Moreover, although the number of cycles is limited, the data show a promising level of stability, with no evident degradation. Representative individual cycles collected for these conditions are presented in Figure 5A, along with the results from M6 (Table 1), whereas Figure 5B shows the cumulative hydrogen production values as averaged over all 14 cycles. These three sets of experiments differ only in terms of the sample mass and the reduction gas flow rates, parameters that are rarely reported in the literature, yet the differences in fuel productivity are stark. The combination, for example, of halving the oxide mass, from 0.5215 to 0.2559 g, and doubling the reduction gas flow rate, from 500 to 1,000 mL min^{-1} (M4 versus M7), results in a 50% increase in the cumulative hydrogen produced, from 6.8 ± 0.1 to 10.0 ± 0.2 mL g^{-1} , over the otherwise identical 1.5-h cycles. The impact of changing these seemingly benign process parameters on the peak hydrogen production rate is particularly strong, causing this term to more than double (Table 1). It must be recognized, however, that the decrease in mass is accompanied by a decrease in the absolute hydrogen production. The impact of doubling the reduction gas flow rate alone (without changing sample mass) has a less pronounced effect on the mass normalized productivity, causing an increase of just over 10% (M4 versus M6). The sample mass is a more critical parameter than V_{TR} for fuel productivity because it changes the gas

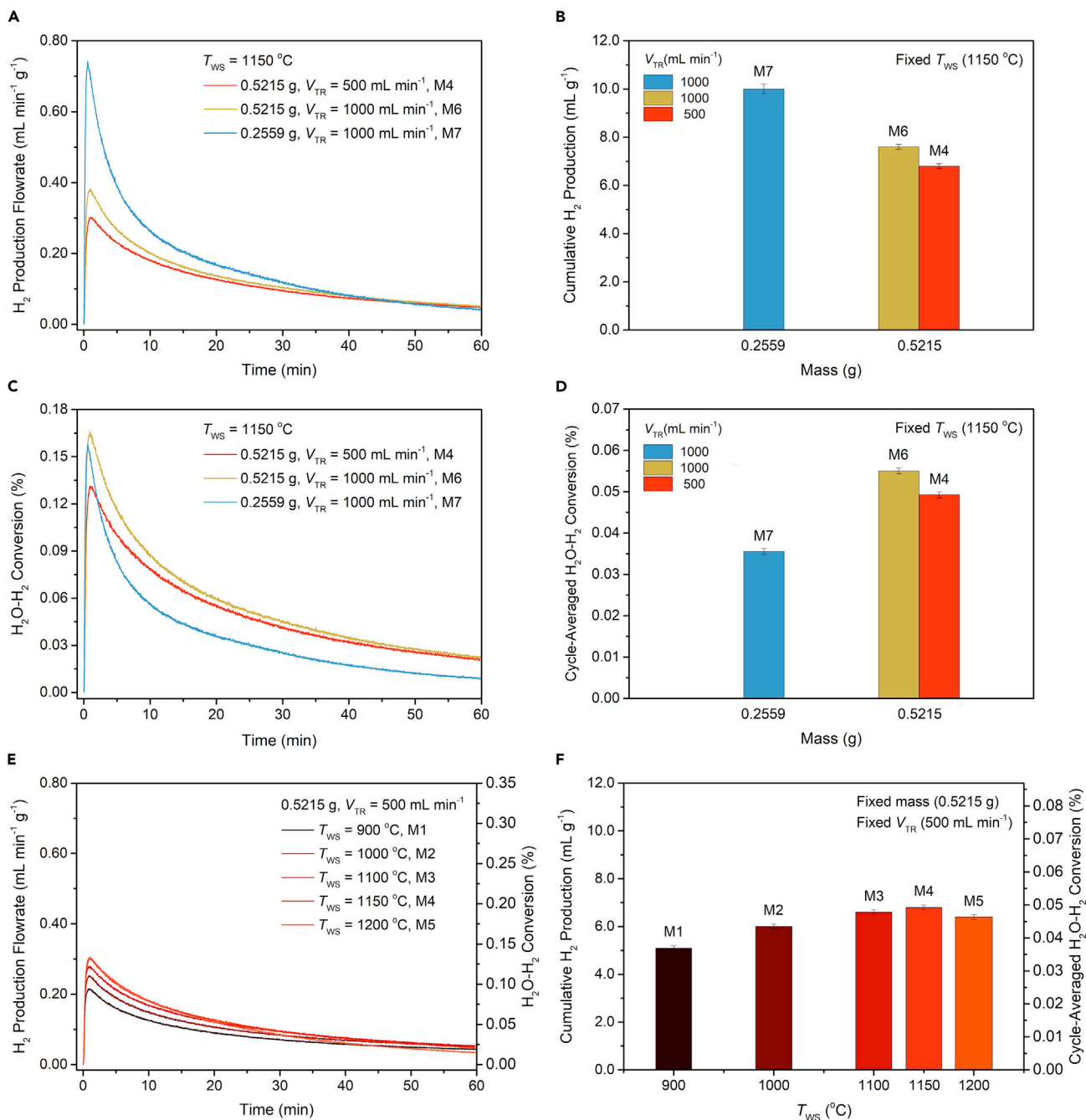


Figure 5. Impact of Process Parameters on Hydrogen Productivity and Production Rate

Impact of sample mass and thermal reduction gas flow rate in thermochemical cycling on the hydrogen production behavior of porous monolithic CTM55 with all other parameters held fixed: (A) instantaneous hydrogen production flow rates; (B) cumulative hydrogen production; (C) steam-to-hydrogen conversion profiles; (D) cycle-averaged steam-to-hydrogen conversion. Impact of water-splitting temperatures on the hydrogen production behavior with all other parameters held fixed: (E) instantaneous hydrogen production flow rates (left axis) and steam-to-hydrogen conversion profiles (right axis); (F) cumulative hydrogen production (left axis) and cycle-averaged steam-to-hydrogen conversion (right axis). Full details of the experimental cycling conditions are given in Table 1. Error bars in (B), (D), and (F) are the estimated standard deviations from averaging over 14 individual cycles for each condition.

flow rate per unit of oxide for both half-cycles. These results reveal the overwhelming need to carry out process optimization and material comparisons under conditions in which all parameters are controlled. We further note that the fuel productivity of

$10.0 \pm 0.2 \text{ mL g}^{-1}$ obtained from CMT55 under the favorable conditions of small mass and high gas flow rate exceeds by a wide margin the value of 6.9 mL g^{-1} obtained from $\text{La}_{0.6}\text{Sr}_{0.4}\text{Mn}_{0.6}\text{Al}_{0.4}\text{O}_{3-\delta}$ ²⁵ at the same T_{TR} . Moreover, the smaller temperature swing, 200°C versus 350°C , implies relaxed requirements for solid-state heat recovery in the design of an efficient reactor.

Beyond hydrogen produced per unit oxide, the quantity of hydrogen produced per unit water, i.e., the steam-to-hydrogen molar conversion, has emerged as an important parameter for characterizing STCH cycles.^{26,27} The conversion, like the hydrogen productivity, is high at the initiation of the fuel production half-cycle and falls toward zero as the reaction nears completion (Figure 5C). A comparison of the cycle-averaged conversion rate (Figure 5D) with the cumulative hydrogen production (Figure 5B) reveals the trade-off between these two parameters: a small quantity of oxide in a large volume of steam results in high productivity per unit oxide and low conversion, and vice versa.

Turning to a more conventionally considered parameter, the results of varying T_{WS} in the multi-cycle experiments, with all other parameters held fixed, are presented in Figures 5E and 5F. Reported again are the profiles obtained for the third cycle, along with the cumulative hydrogen production values as averaged over all 14 cycles. Here it is evident that the cumulative fuel production peaks at $T_{\text{WS}} = 1,150^\circ\text{C}$, with the maximum rate of instantaneous hydrogen production peaking at a slightly higher temperature. Furthermore, because the sample mass and gas flow rates are fixed across the five different sets of cycles, the steam-to-hydrogen conversion follows exactly the fuel productivity trend (as also reported in Figures 5E and 5F). For a process limited entirely by thermodynamics, a decrease in T_{WS} will result in a monotonic increase in the rate of fuel production because decreasing temperature causes $\Delta_{\text{rxn}}G$ of the water-splitting reaction (Equation 2) to become more negative. Strictly, the statement applies for a given oxygen non-stoichiometry, a characteristic which may vary across cycling experiments with different δ_{f} resulting from the differing T_{WS} . However, for the range of T_{WS} values considered, this effect is small. A process limited entirely by kinetics, on the other hand, will monotonically benefit from an increase in temperature. The results thus indicate that the water-splitting step on the porous CTM55 prepared here is increasingly dominated by material kinetics at temperatures below $1,150^\circ\text{C}$ and increasingly by thermodynamics at temperatures above $1,150^\circ\text{C}$, with contributions from both factors affecting the outcome at intermediate temperatures. Analogous behavior has been observed in ceria.²⁸

A direct comparison of all of the cycling conditions is provided in Figure S19. Particular emphasis is placed on the dramatic role of sample mass in establishing the metrics of both H_2 productivity per unit of oxide and steam-to-hydrogen conversion. The results underscore the importance of developing experimental protocols that enable meaningful comparisons between candidate STCH materials.

Single Cycles for Predictable Gas Production

The influence of water-splitting temperature on the multi-cycle experiments suggests gas-phase mass transport limitations on the overall gas production behavior, particularly at high temperatures. This possibility was explored using an experimental protocol, detailed in Figure S20, in which reduction and oxidation were performed from well-defined initial conditions. In brief, the sample mass was 0.5215 g and full oxidation was achieved before cycling via relevant pretreatment steps. With reduction conditions kept fixed, two different water-splitting conditions were explored. Specifically, thermal reduction was carried out upon heating from ambient

temperature at a rate of $400^\circ\text{C min}^{-1}$ to $T_{\text{TR}} = 1,350^\circ\text{C}$ (nominal) and held for $t_{\text{TR}} = 0.5$ h, with $p\text{O}_2^{\text{TR}} = 10^{-5}$ atm (nominal) and $V_{\text{TR}} = 500$ mL min^{-1} throughout the heating and hold periods. The subsequent water-splitting step was carried out with all conditions except V_{WS} held the same. The fixed conditions were set at $T_{\text{WS}} = 1,000^\circ\text{C}$ and $p\text{H}_2\text{O}^{\text{WS}} = 0.4$ atm. The hydrogen evolution was tracked for 3 h. The two V_{WS} values were 200 and 300 mL min^{-1} . Shown alongside the experimental results are the computed profiles expected for a process in which the oxide remains in quasi-equilibrium with the gas phase throughout the oxygen loss and uptake half-cycles.

The gas evolution profiles for quasi-equilibrium (or equivalently, thermo-kinetic) behavior were computed using a mass balance model presented previously.²⁹ The prediction applies under the following conditions: the temperature across the oxide is spatially invariant; the composition of the gas in the vicinity of the porous oxide is also spatially invariant; and the rate of reaction on the oxide surface and that of oxide transport through the solid are both fast relative to the rate at which the gas is supplied. The first two conditions are easily met by ensuring that the sample volume is small relative to the hot zone of the reactor and by fabricating an oxide structure with high porosity. The analysis as implemented here further assumes that the thermodynamic functions, $\Delta_{\text{red}}H^\ominus(\delta)$ and $\Delta_{\text{red}}S^\ominus(\delta)$, are temperature invariant, an assumption justified by linearity of the curves in the van't Hoff plot, [Figure 3B](#). Comparison of the computed and measured profiles can then provide insight into the role of material kinetics on gas evolution rates. As shown elsewhere,²⁹ the rate of change of the oxygen non-stoichiometry during the reduction and the water-splitting half-cycles are, respectively, given as

$$\frac{d\delta_{\text{red}}}{dt} = \frac{2F_{\text{TR}}}{n_{\text{oxide}}} \frac{(p\text{O}_2(\delta, T_{\text{TR}}) - p\text{O}_2^{\text{TR}})}{(p_{\text{tot}} - p\text{O}_2(\delta, T_{\text{TR}}))} \quad (\text{Equation 5})$$

and

$$\frac{d\delta_{\text{ox}}}{dt} = \frac{F_{\text{WS}}}{n_{\text{oxide}}} \frac{2p\text{O}_2(\delta, T_{\text{WS}})^{\frac{3}{2}}/p_{\text{ref}}^{\frac{1}{2}} + 2p\text{O}_2(\delta, T_{\text{WS}})K_{\text{H}_2\text{O}, T_{\text{WS}}} - \chi_{\text{H}_2\text{O}}K_{\text{H}_2\text{O}, T_{\text{WS}}}(p_{\text{tot}} - p\text{O}_2(\delta, T_{\text{WS}}))}{(p\text{O}_2(\delta, T_{\text{WS}})^{\frac{1}{2}}/p_{\text{ref}}^{\frac{1}{2}} + K_{\text{H}_2\text{O}, T_{\text{WS}}})(p_{\text{tot}} - p\text{O}_2(\delta, T_{\text{WS}}))} \quad (\text{Equation 6})$$

where F_{TR} and F_{WS} are the molar flow rates of the gases in thermal reduction step and water-splitting steps, respectively, n_{oxide} is the number of moles of metal oxide, $\chi_{\text{H}_2\text{O}}$ is the fraction of steam in the gas supplied in the water-splitting step, $K_{\text{H}_2\text{O}}$ is the equilibrium thermolysis reaction constant, p_{tot} is the total pressure (typically 1 atm), and $p\text{O}_2(\delta, T)$ describes the relationship between the instantaneous $p\text{O}_2$ and δ at the reaction temperature as given from [Equation 4](#). The more typically reported volumetric gas flow rates are $V_{\text{TR}} = F_{\text{TR}} \times$ (reduction gas molar volume) and $V_{\text{WS}} = F_{\text{WS}} \times$ (oxidation gas molar volume). For ease of discussion, the oxide mass normalized flow rates of the reaction gases, \bar{V}_{TR} and \bar{V}_{WS} , are introduced and defined as the volumetric flow rates divided by the oxide mass. The temperature ramp during reduction is readily treated by applying an appropriate increment in temperature with each time step of the calculation.²⁸ For all simulations, the time step was set at 0.01 min.

The measured oxygen evolution profile is captured relatively well by the predictions of the thermo-kinetic model, where the calculation is carried out using the measured $p\text{O}_2^{\text{TR}}$ of 2.66×10^{-5} atm rather than the nominal value of 10^{-5} atm ([Figure S21A](#)). A slight disagreement at low temperature, $\sim 500^\circ\text{C}$, is likely due to a small overshoot in

the temperature heating profile, whereas the slight disagreement at $\sim 800^\circ\text{C}$ is due to the inability of the model to account for the crystallographic phase transition. A substantive, although still relatively small, deviation between the predicted and measured oxygen profiles emerges at a temperature of $\sim 950^\circ\text{C}$ (Figure S21B). The lag in the experimentally measured oxygen evolution suggests a material kinetic limitation at this intermediate temperature. However, after no more than several minutes of reduction at $1,350^\circ\text{C}$, the experimental profile recovers to the value of the predicted profile, and the cumulative experimental oxygen production after 0.5 h of reduction matches the value of 18.3 mL g^{-1} computed by the model.

The results indicate that, at moderate temperatures and when the thermodynamic driving force for reduction is high, kinetic factors co-limit the oxygen evolution rate, with thermodynamic factors becoming dominant at high temperatures. Three additional important points also emerge. First, a reduction time of 0.5 h yields a change in oxygen non-stoichiometry that is 97% of the equilibrium value. Thus, the multi-cycle experiments benefitted from oxygen release to near equilibrium extents. Second, the oxygen release is far greater in the early part of the reduction half-cycle than the latter part, suggesting that perhaps a 10 min reduction time, which yields 17.4 mL g^{-1} (95% of that obtained after 30 min), would produce satisfactory cycling results. It is not immediately obvious, however, whether such a strategy would be successful because a decrease in δ_f would decrease the driving force for subsequent water splitting, penalizing the hydrogen production rate. Furthermore, in reduction cycles that follow water splitting, the reduction will initiate at $\delta > 0$, and may not benefit from such favorable kinetics. Third, in both the experimental and computed results a small anomaly occurs in the very initial stages of oxygen release. As already alluded to, this reflects the orthorhombic to cubic phase change. Because this transition occurs at too low a δ to be relevant in realistic cycles, no attempt was made to more accurately simulate the effect.

As with reduction, the general features of the experimental hydrogen production profiles (Figures 6C and 6D) were captured by the thermo-kinetic model. In particular, the strong impact of oxidation gas flow rate, a prediction of the model, is a clear indication that the supply of H_2O contributes to limiting the overall reaction rate. Although the model and the experiment broadly agree, there is some disagreement between the two, particularly at the initial stages of the water-splitting half-cycle when the reaction rate is highest. Such disagreement reveals that material kinetic factors must play a co-limiting role. The transition between thermodynamic (gas-phase mass transport) limitations and material kinetic limitations is known to be not only a function of mass normalized gas flow rates and temperature, but also material architecture, because the latter fixes the available surface area for the reaction and in principle also the oxygen solid-state diffusion lengths. For the particular form of CTM55 used here, it can be concluded that hydrogen evolution is co-limited by thermodynamic and kinetic factors at a water-splitting temperature of $1,000^\circ\text{C}$ and \bar{V}_{WS} of $384\text{--}575\text{ mL min}^{-1}\text{ g}^{-1}$. This result is in agreement with the multi-cycle experiments, in which the impact of kinetic limitations began to emerge at $T_{\text{WS}} = 1,100^\circ\text{C}$ (with $\bar{V}_{\text{WS}} = 575\text{ mL min}^{-1}\text{ g}^{-1}$). It is further noteworthy that the low rate of the water-splitting reaction results in a cumulative hydrogen production that is less than 60% of the equilibrium value, even after 3 h of accumulation. The very slow rate detected beyond about 1 h of reaction time is largely a consequence of the weak driving force, rather than poor material kinetics. On the other hand, in experiments in which gas flow rates are made so high that thermodynamic limitations can be fully ignored, it may be possible to determine kinetic parameters.^{30,31} It has been shown that, under such conditions, the surface reaction rather than diffusion of oxygen through the material bulk is the rate-controlling material

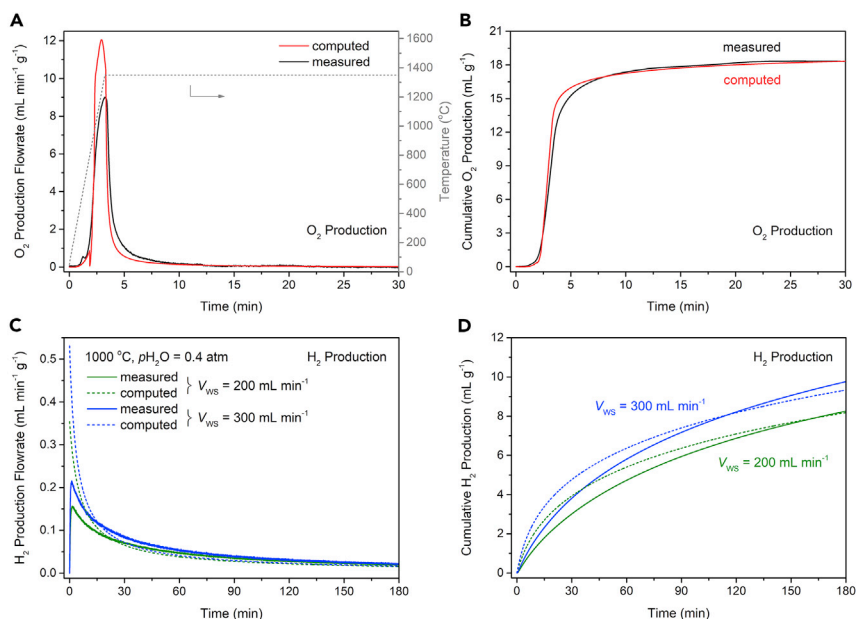


Figure 6. Experimental and Predicted Gas Evolution Characteristics over CTM55 during Thermochemical Water Splitting Experiments

Data are for a porous monolithic, 0.5215 g in mass and fully oxidized material at the initiation of thermal reduction. See text for description of the model and [Figures S20](#) and [S21](#) for complete experimental details. Computed and measured (A) instantaneous O_2 flowrate; (B) cumulative O_2 evolution; (C) instantaneous H_2 flowrate; and (D) cumulative H_2 production. The final oxygen non-stoichiometry value after 0.5 h of thermal reduction is ~ 0.23 , and this value is used as an input for the calculation of the H_2 production profiles.

phenomenon.^{27,28,32} It is of some note that both the model and experiment reveal that hydrogen production is possible from a non-stoichiometric oxide with an enthalpy of reduction that is smaller than the enthalpy of the steam thermolysis reaction,¹¹ albeit with a relatively small steam-to-hydrogen conversion ratio.

Evaluation of the porous CTM55 after the completion of the suite of thermochemical cycling experiments revealed that neither the crystal structure nor the microstructure was impacted by the process ([Figure S22](#)). The orthorhombic perovskite phase was detected by X-ray powder diffraction following a final re-oxidation in air at 1,000°C, and the porous structure was retained without evident coarsening or grain growth, consistent with the robust cycling behavior reported in [Figures 4](#) and [S14–S18](#).

Comparison with Related Materials

While recognizing that fuel production metrics can be manipulated by changing seemingly unimportant process parameters, it is nevertheless valuable to place the hydrogen production achieved with CTM55 in the context of previous literature results. Here, we consider fuel production per cycle per unit of oxide (mL g^{-1}) and also the cycle-averaged fuel production rate ($\mu\text{L min}^{-1} \text{g}^{-1}$) as critical metrics. Comparison with previous literature^{18,25,33–35} ([Figure 7](#)) shows that CTM55 provides perhaps the most attractive combination of these two measures of all materials reported. Details of the experimental conditions of the studies reported in the figure are provided in [Table 2](#). In light of the thermodynamic similarities between CTM55 and STM55 ([Figure 3](#)), the higher productivity of the former immediately implies material kinetic and/or morphological differences, particularly because the water-splitting step for CTM55 was carried out at a slightly higher and therefore thermodynamically less favorable temperature (1,150°C)

Table 2. Summary of the Thermochemical Water Splitting Conditions Used in Literature Studies and Compared with the Present Work

Material	Sample Mass (g)	Sample Form	Porosity (%)	T_{TR} ($^{\circ}\text{C}$)	Reduction			Oxidation Gas (atm)		t_{WS} (min)	H_2 Yield (mL g^{-1})	Source, Ref. no.
					Gas ($\rho\text{O}_2/\text{atm}$)	t_{TR}^{a} (min)	T_{WS} ($^{\circ}\text{C}$)	pH_2O	pO_2^{b}			
$\text{CaTi}_{0.5}\text{Mn}_{0.5}\text{O}_{3-\delta}$	0.2559	monolith	50	1,350	10^{-5} (in Ar)	30	1,150	0.4	2.5×10^{-5}	60	10.0	This work
$\text{SrTi}_{0.5}\text{Mn}_{0.5}\text{O}_{3-\delta}$	0.5225	monolith	51	1,400	10^{-5} (in Ar)	30	1,100	0.4	1.5×10^{-5}	60	8.3	Qian et al. ¹⁸
$\text{SrTi}_{0.5}\text{Mn}_{0.5}\text{O}_{3-\delta}$	0.2529	monolith	51	1,350	10^{-5} (in Ar)	30	1,100	0.4	1.5×10^{-5}	60	7.4	Qian et al. ¹⁸
$\text{BaCe}_{0.25}\text{Mn}_{0.75}\text{O}_{3-\delta}$	~0.1	powder	–	1,400	UHP Ar	5.5	1,000	0.4	4.8×10^{-6}	20	4.1	Barcellos et al. ³⁴
$\text{BaCe}_{0.25}\text{Mn}_{0.75}\text{O}_{3-\delta}$	~0.1	powder	–	1,350	UHP Ar	5.5	1,000	0.4	4.8×10^{-6}	20	3.3	Barcellos et al. ³⁴
$\text{LaGa}_{0.4}\text{Co}_{0.6}\text{O}_{3-\delta}$	0.5	powder	–	1,350	HP ^c Ar	132.5	800	1	4.7×10^{-7}	400	10.7	Chen et al. ³⁶
$\text{La}_{0.6}\text{Sr}_{0.4}\text{MnO}_{3-\delta}$	0.51	monolith	59	1,400	10^{-5} (in Ar)	70	800	0.2	1.6×10^{-7}	60	8.9	Ignatowich et al. ¹⁷ , Yang et al. ³³
$\text{La}_{0.7}\text{Sr}_{0.3}\text{MnO}_{3-\delta}$	0.53	monolith	58	1,400	10^{-5} (in Ar)	60	800	0.2	1.6×10^{-7}	31	5.7	Ignatowich et al. ¹⁷ , Yang et al. ³³
$\text{La}_{0.6}\text{Sr}_{0.4}\text{Mn}_{0.6}\text{Al}_{0.4}\text{O}_{3-\delta}$	~0.1	powder	–	1,350	He	30	1,000	0.4	4.8×10^{-6}	30	6.9	McDaniel et al. ²⁵
$\text{La}_{0.6}\text{Ca}_{0.4}\text{Mn}_{0.6}\text{Al}_{0.4}\text{O}_{3-\delta}$	~0.5	monolith	NA	1,400	HP Ar	140	1,000	~0.4	$\sim 4.8 \times 10^{-6}$	60	9.6	Wang et al. ³⁷
$(\text{FeMgCoNi})\text{O}_x$	~0.1	fine powder	–	1,300	UHP Ar	300	800	0.24 ^d	4.7×10^{-13}	300	10.1	Zhai et al. ³⁵
$(\text{FeMgCoNi})\text{O}_x$	~0.2	sintered pieces	–	1,300	UHP Ar	30	800	0.24 ^d	4.7×10^{-13}	60	5.5	Zhai et al. ³⁵

^aReduction time includes the heating/cooling time between thermal reduction and water-splitting temperatures, in addition to the time of the isothermal hold at the thermal reduction temperature.

^bOxygen partial pressure expected from the equilibration of the gas-phase thermolysis reaction.

^cHP, high purity; UHP, purity.

^dWith additional hydrogen supplied to yield $\text{pH}_2:\text{pH}_2\text{O} = 1:1,045$.

Data are plotted in Figure 7.

than in the case of STM55 (1,100 $^{\circ}\text{C}$). As discussed in the context in Figure 5E, material kinetic parameters begin to impact the hydrogen evolution rate of CTM55 at about 1,150 $^{\circ}\text{C}$. Even after accounting for a decrease by ~3% in hydrogen productivity for CTM55 had water splitting been carried out at 1,100 $^{\circ}\text{C}$ (by analogy to the different results from conditions M3 and M4), CTM55 provides higher fuel productivity for finite-time cycles than STM55. Thus, despite the non-negligible limitation introduced by the surface reaction step in CTM55, the fuel production rate is nevertheless more favorable than in STM55. Further studies are required to establish whether the benefit derives from an inherently higher surface reaction rate or a higher specific surface area in the CTM55 sample examined. Surface reaction kinetics and sample morphology are likely to also have affected the fuel production performance obtained for the other materials reported in Figure 7. Indeed, in the case of $\text{LaGa}_{1-y}\text{Co}_y\text{O}_{3-\delta}$ materials, the beneficial role of Ir as a catalyst in the water-splitting half-cycle was demonstrated,³⁶ implying the prevalence of kinetic limitations which alternatively could plausibly be overcome via microstructural engineering.

Conclusions

We demonstrate that the perovskite $\text{CaTi}_{0.5}\text{Mn}_{0.5}\text{O}_3$ (CTM55) has exceptional capacity for hydrogen production via thermochemical cycling. The material undergoes an orthorhombic to cubic transition at small δ , and remains in the cubic phase regime throughout typical, high-temperature cycling conditions. Within the cubic regime, the material has an ideal combination of high entropy and moderate enthalpy. In comparison with CaMnO_3 , CTM55 transforms to the cubic phase at smaller δ and displays a higher enthalpy, without a decrease in entropy. Furthermore, these changes occur despite the apparent redox inactivity of Ti, which appears to retain the 4+ oxidation state throughout the cycling, including complete reduction to form CaTiO_3 and MnO . Regardless of the fundamental materials chemistry underlying the properties of CTM55, and in particular the role of the redox inactive Ti^{4+} dopant, the thermodynamic

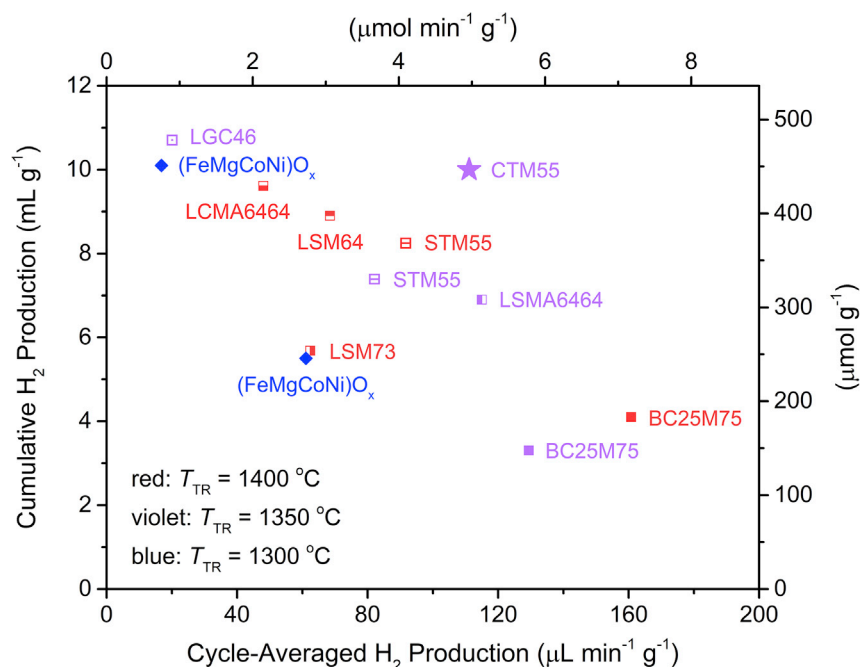


Figure 7. Comparison of the Thermochemical Hydrogen Productivity Measured from CTM55 (Star, This Work) to That of Other Reported Promising Materials

Literature data are from the perovskites (square data points) $\text{SrTi}_{0.5}\text{Mn}_{0.5}\text{O}_{3-\delta}$ (STM55),¹⁸ $\text{BaCe}_{0.25}\text{Mn}_{0.75}\text{O}_{3-\delta}$ (BC25M75),³⁴ $\text{LaGa}_{0.4}\text{Co}_{0.6}\text{O}_{3-\delta}$ (LGC46),³⁶ $\text{La}_{0.6}\text{Sr}_{0.4}\text{MnO}_{3-\delta}$ (LSM64),³³ $\text{La}_{0.7}\text{Sr}_{0.3}\text{MnO}_{3-\delta}$ (LSM73),³³ $\text{La}_{0.6}\text{Sr}_{0.4}\text{Mn}_{0.6}\text{Al}_{0.4}\text{O}_{3-\delta}$ (LSMA6464),²⁵ and $\text{La}_{0.6}\text{Ca}_{0.4}\text{Mn}_{0.6}\text{Al}_{0.4}\text{O}_{3-\delta}$ (LCMA6464),³⁷ and the poly-cation oxide (diamond data points) $(\text{FeMgCoNi})\text{O}_x$,³⁵ under the cycling conditions indicated. This representation of the data underscores the challenges of attaining both a high cumulative hydrogen production quantity and a high production rate (as averaged over the complete cycle time).

characteristics of this perovskite are well suited to thermochemical fuel production. Shown in this work is also the sensitivity of fuel production profiles to gas flow rate and sample mass, parameters that are rarely reported. This sensitivity naturally arises when the material is limited or co-limited by the magnitude of the thermodynamic driving force for the reaction. Because the driving force is greatest at the initiation of either oxygen release or water-splitting reactions, material kinetic factors have greater impact on peak rates than cumulative productivity. Furthermore, because water splitting is typically carried out at a temperature lower than thermal reduction, material kinetic effects are more prevalent as rate-limiting factors for the water-splitting step. The co-limitation of CTM55 by thermodynamic and kinetic factors in the sluggish hydrogen evolution reaction indicates that surface engineering and/or material architectural design can, to some degree, enhance the fuel productivity, particularly if one wishes to implement very short cycles. Such steps will inherently also improve the steam-to-hydrogen conversion, but this metric remains a major challenge facing the technological realization of STCH approaches to solar energy storage.

EXPERIMENTAL PROCEDURES

Resource Availability

Lead Contact

Further information and requests for resources and materials should be directed to and will be fulfilled by the Lead Contact, Sossina M. Haile (sossina.haile@northwestern.edu).

Materials Availability

This study did not generate new, unique reagents.

Data and Code Availability

The published article includes all data analyzed during this study.

Material Synthesis

The material CTM55 was prepared by solid-state reaction (SSR) in which stoichiometric amounts of CaCO_3 (ACS reagent, $\geq 99.0\%$, powder, Sigma-Aldrich), TiO_2 ($\geq 99.8\%$ trace metal basis, Sigma-Aldrich), and MnO_2 (Reagent Plus, $\geq 99\%$, Sigma-Aldrich) were mixed with isopropanol (ACS reagent, $\geq 99.5\%$, Sigma-Aldrich). The slurry mixture was hand milled, then formed into a disc under 20 MPa of uniaxial pressure for 1 min. Calcination was then carried out at $1,250^\circ\text{C}$ for 24 h under still air. The resulting material was ground for XRD measurements, which showed incomplete reaction. The material was then formed into a disc again and held at a reaction temperature of $1,400^\circ\text{C}$ for 24 h. These steps were repeated until no further changes were observed in the diffraction pattern. The resulting bulk powders were used for subsequent analysis of crystal structure and chemical composition. A portion of the powders (0.25–1.6 g) was mixed with isopropanol and hand-pressed into cylindrical pellets, which were then sintered at $1,400^\circ\text{C}$ for 2 h to form porous monoliths ($\sim 50\%$ porosity) used for thermal analysis and thermochemical water-splitting experiments.

PLD of Thin Films

The perovskite thin film used for XANES characterization was deposited on an R-cut single crystal sapphire substrate ($10 \times 10 \text{ mm}^2$, MTI Corporation) by PLD using a PVD PLD/MBE 2300 in the PLD core facility at Northwestern University. A sufficiently dense ($\sim 97\%$) PLD target of CTM55 was prepared from the SSR-prepared powder by uniaxial pressing (20 MPa, 1 min) followed by isostatic pressing (250 MPa, 20 min) and sintering at $1,400^\circ\text{C}$ for 24 h under flowing oxygen. Film growth was performed out using a 248-nm KrF laser with 270 mJ per pulse at a repetition rate of 5 Hz for a total count of 7,500 pulses. The calibrated substrate temperature was 700°C (ramp rate, $10^\circ\text{C min}^{-1}$), and the chamber $p\text{O}_2$ was 30 mTorr. Upon completion of film growth, the PLD chamber was vented to achieve a $p\text{O}_2$ of 300 Torr to oxidize the film, and was then slowly cooled at 5°C min^{-1} .

Physical Characterization and Chemical Analysis

Ex situ X-ray powder diffraction studies were performed using a Rigaku Ultima IV diffractometer using $\text{Cu K}\alpha$ ($\lambda = 0.1541 \text{ nm}$) radiation (40 kV, 44 mA), and data collected over the 2θ range 20° – 80° at a step size of 0.05° and a scanning speed of 5° min^{-1} . Details of the high-temperature treatment for *ex situ* stability measurements are provided in the [Supplemental Information](#). *In situ* high-temperature diffraction data were collected on the same diffractometer with the same data collection parameters using an Ultima HTK 1200 heating chamber to achieve the desired temperatures. A dwell time of 22 min at each measurement temperature was implemented to attain equilibrium. Phase formation and structure evolution in both *ex situ* and *in situ* measurements were analyzed using the whole pattern fitting function implemented in the commercial software program JADE (Materials Data). Crystallographic parameters were analyzed by Rietveld refinement using the GSAS-II Crystallography Data Analysis Software package. Details of the crystallographic characterization of the films used for the XANES study are given in the [Supplemental Information](#). Electron microscopy was performed using a field emission scanning electron microscope (Hitachi SU8030) under an acceleration voltage of 20 kV. EDS data for chemical analysis were collected using an Oxford AZtec X-Max 80 silicon

drift detector. Quantitative chemical analysis by ICP-OES was carried out using a Thermo Fisher Scientific iCAP7000 analyzer. Approximately ~5 mg of powder was dissolved in a solution of 5% aqua regia. The solution was held for 48 h at room temperature and then heated in a water bath at 65°C for 30 min to assure complete dissolution of the powder.

Thermal Analysis of Bulk Material

Both simultaneous TG-DSC and TG only measurements were performed using a Netzsch STA 449 C Jupiter thermal analyzer with the sample placed in a platinum pan. The gas atmosphere was fixed by mixing gases (Ar and premixed Ar + O₂ gases) supplied using digital mass flow controllers. The $p\text{O}_2$ in the exhaust gas was monitored using an *in situ* $p\text{O}_2$ sensor (Micropas, Sentag), held in a sealed quartz tube in a furnace at a temperature of 700°C. For TG-DSC measurements the mass of the porous sample was 174.68 mg, whereas for the complete reduction TG experiment it was 657.21 mg. For the measurement of redox thermodynamics by TG, the mass was either 1.604 or 0.945 g, as described in the main text.

High-Temperature *In Situ* XANES Measurements

XANES measurements were carried out at the DuPont-Northwestern-Dow Collaborative Access Team. An Anton Paar (DHS 1100) dome apparatus was used for *in situ* heating to achieve the measurement temperatures. Data were collected under a flow of synthetic air supplied at a rate of 50 mL min⁻¹. The incidence angle of the incoming beam was set at $\alpha = 7^\circ$, at which point the penetration depth exceeds the 200 nm thickness of the films, but the film is thin enough to avoid self-absorption effects. The reference powders, TiO₂, Ti₂O₃, MnO₂, and MnO, were uniformly spread on adhesive tapes, which were then folded a few times to minimize occurrence of any pin holes. These were measured in transmission mode. Analysis of the spectra was performed using the ATHENA package in the Demeter X-ray absorption spectroscopy data analysis software. Further experimental details are provided in the [Supplemental Information](#).

Thermochemical Water-Splitting Measurements

The gas production from water splitting was measured in an in-house constructed thermochemical cycling station comprising an infrared gold imaging furnace (ULVAC RHL-E44VHT) capable of rapid heating and cooling of materials. The station is equipped with a manifold of MFCs to control the flow rate of inlet gases, a quadrupole mass spectrometer (Pfeiffer Thermostar GSD301T2) for off-gas detection, and a high-temperature $p\text{O}_2$ sensor (Micropas, Sentag) for *in situ* measurement of $p\text{O}_2$. The reactor in which water splitting took place was composed of one outer quartz tube (1/2" in diameter) and one inner alumina tube (1/4" in diameter). To ensure blackbody heating of the sample and thermocouples, the inside of the alumina tube was lined along 3 cm of the central region with two layers of platinum foil (99.9% purity, 0.025 mm thick, Alfa Aesar). A sintered porous cylindrical sample with a mass of ~0.5 g was shaped to match that of the 1/4" diameter of the inner tube and then placed in the hot zone of the reactor. An alumina-sheathed S-type thermocouple, the tip of which was in contact with the upstream end of the sample, was used to control the temperature. Complete details of the gas flow protocols for the cycling experiments of [Table 1](#) and [Figures 4, 5, and 6](#) are provided in the [Supplemental Information](#).

SUPPLEMENTAL INFORMATION

Supplemental Information can be found online at <https://doi.org/10.1016/j.matt.2020.11.016>.

ACKNOWLEDGMENTS

This research is funded by the U.S. Department of Energy, through the office of Energy Efficiency and Renewable Energy (EERE) contract DE-EE0008089. The support from the European Union's Horizon 2020 Research And Innovation Programme under the Marie Skłodowska-Curie grant agreement no. 746167 is also acknowledged. This work made use of the Jerome B. Cohen X-Ray Diffraction Facility and the Pulsed Laser Deposition Shared Facility at the Materials Research Center at Northwestern University supported by the National Science Foundation MRSEC program (DMR-1720139) and the Soft and Hybrid Nanotechnology Experimental (SHyNE) Resource (NSF ECCS-1542205). This work additionally made use of the DuPont-Northwestern-Dow Collaborative Access Team (DND-CAT) located at Sector 5 of the Advanced Photon Source (APS) supported by Northwestern University, The Dow Chemical Company, and DuPont de Nemours, Inc. The APS is a U.S. Department of Energy (DOE) Office of Science User Facility operated for the DOE Office of Science by Argonne National Laboratory under contract no. DE-AC02-06CH11357. The authors acknowledge Dr. Timothy Davenport and Dr. Stephen Wilke for help in thermochemical hydrogen production measurements, and graduate student Louis Wang for assistance with Rietveld refinements and for consultation on thermogravimetric measurements.

AUTHOR CONTRIBUTIONS

X.Q. performed the majority of the experiments and their analysis. J.H. and B.B performed atomistic calculations. E.M. assisted with thermal analysis and W.Y. assisted with XANES measurements. C.W. supervised atomistic computational studies. S.M.H. and C.W. designed the research plan, with S.M.H. providing overall guidance for the research work. X.Q. and S.M.H. wrote the manuscript with input from all authors.

DECLARATION OF INTERESTS

The authors declare no competing interests.

Received: July 29, 2020

Revised: September 29, 2020

Accepted: November 24, 2020

Published: December 22, 2020

REFERENCES

1. Tachibana, Y., Vayssieres, L., and Durrant, J.R. (2012). Artificial photosynthesis for solar water-splitting. *Nat. Photon.* 6, 511–518.
2. Young, K.J., Martini, L.A., Milot, R.L., Snoeberger, R.C., Batista, V.S., Schmuttenmaer, C.A., Crabtree, R.H., and Brudvig, G.W. (2012). Light-driven water oxidation for solar fuels. *Coord. Chem. Rev.* 256, 2503–2520.
3. Scheffe, J.R., and Steinfeld, A. (2014). Oxygen exchange materials for solar thermochemical splitting of H_2O and CO_2 : a review. *Mater. Today* 17, 341–348.
4. Bulfin, B., Vieten, J., Agrafiotis, C., Roeb, M., and Sattler, C. (2017). Applications and limitations of two step metal oxide thermochemical redox cycles; a review. *J. Mater. Chem. A* 5, 18951–18966.
5. Chueh, W.C., Falter, C., Abbott, M., Scipio, D., Furler, P., Haile, S.M., and Steinfeld, A. (2010). High-flux solar-driven thermochemical dissociation of CO_2 and H_2O using nonstoichiometric ceria. *Science* 330, 1797–1801.
6. Scheffe, J.R., and Steinfeld, A. (2012). Thermodynamic analysis of cerium-based oxides for solar thermochemical fuel production. *Energy Fuels* 26, 1928–1936.
7. Kubicek, M., Bork, A.H., and Rupp, J.L.M. (2017). Perovskite oxides—a review on a versatile material class for solar-to-fuel conversion processes. *J. Mater. Chem. A* 5, 11983–12000.
8. Vieten, J., Bulfin, B., Huck, P., Horton, M., Guban, D., Zhu, L., Lu, Y., Persson, K.A., Roeb, M., and Sattler, C. (2019). Materials design of perovskite solid solutions for thermochemical applications. *Energy Environ. Sci.* 12, 1369–1384.
9. Meredig, B., and Wolverton, C. (2009). First-principles thermodynamic framework for the evaluation of thermochemical H_2O - or CO_2 -splitting materials. *Phys. Rev. B* 80, 245119.
10. Wolverton, C., and Haile, S.M. (2019). Transformative materials for high-efficiency thermochemical production of solar fuels, DOE Hydrogen and Fuel Cells Annual Merit Review Proceedings (Project ID P167). https://www.hydrogen.energy.gov/pdfs/review19/p167_wolverton_2019_o.pdf.
11. Bulfin, B., Vieten, J., Starr, D.E., Azarpira, A., Zachäus, C., Hävecker, M., Skorupska, K., Schmücker, M., Roeb, M., and Sattler, C. (2017). Redox chemistry of CaMnO_3 and $\text{Ca}_{0.8}\text{Sr}_{0.2}\text{MnO}_3$ oxygen storage perovskites. *J. Mater. Chem. A* 5, 7912–7919.

12. Mastrorlando, E., Qian, X., Coronado, J.M., and Haile, S.M. (2020). The favourable thermodynamic properties of Fe-doped $\text{CaMnO}_{3-\delta}$ for thermochemical heat storage. *J. Mater. Chem. A* 8, 8503–8517.
13. Rormark, L., Morch, A.B., Wiik, K., Stolen, S., and Grande, T. (2001). Enthalpies of oxidation of $\text{CaMnO}_{3-\delta}$, $\text{Ca}_2\text{MnO}_{4-\delta}$ and $\text{SrMnO}_{3-\delta}$ deduced redox properties. *Chem. Mater.* 13, 4005–4013.
14. Deml, A.M., Stevanović, V., Holder, A.M., Sanders, M., O'Hayre, R., and Musgrave, C.B. (2014). Tunable oxygen vacancy formation energetics in the complex perovskite oxide $\text{Sr}_x\text{La}_{1-x}\text{Mn}_y\text{Al}_{1-y}\text{O}_3$. *Chem. Mater.* 26, 6595–6602.
15. Ezbiri, M., Takacs, M., Theiler, D., Michalsky, R., and Steinfeld, A. (2017). Tunable thermodynamic activity of $\text{La}_x\text{Sr}_{1-x}\text{Mn}_y\text{Al}_{1-y}\text{O}_{3-\delta}$ ($0 \leq x \leq 1$, $0 \leq y \leq 1$) perovskites for solar thermochemical fuel synthesis. *J. Mater. Chem. A* 5, 4172–4182.
16. Shi, C.-Y., Hao, Y.-M., and Hu, Z.-B. (2011). Structural and magnetic properties of single perovskite $\text{Ca}(\text{Ti}_{1/2}\text{Mn}_{1/2})\text{O}_3$. *J. Magn. Magn. Mater.* 323, 1973–1976.
17. Ignatowich, M.J., Bork, A.H., Davenport, T.C., Rupp, J.L.M., Yang, C.-K., Yamazaki, Y., and Haile, S.M. (2017). Impact of enhanced oxide reducibility on rates of solar-driven thermochemical fuel production. *MRS Commun.* 7, 873–878.
18. Qian, X., He, J., Mastrorlando, E., Baldassarri, B., Wolverton, C., and Haile, S.M. (2020). Favorable redox thermodynamics of $\text{SrTi}_{0.5}\text{Mn}_{0.5}\text{O}_{3-\delta}$ in solar thermochemical water splitting. *Chem. Mater.* 32, 9335–9346.
19. Panlener, R.J., Blumenthal, R.N., and Garnier, J.E. (1975). A thermodynamic study of nonstoichiometric cerium dioxide. *J. Phys. Chem. Sol.* 36, 1213–1222.
20. Hao, Y., Yang, C.-K., and Haile, S.M. (2014). Ceria-zirconia solid solutions ($\text{Ce}_{1-x}\text{Zr}_x\text{O}_{2-\delta}$, $x \leq 0.2$) for solar thermochemical water splitting: a thermodynamic study. *Chem. Mater.* 26, 6073–6082.
21. Mizusaki, J., Yoshihiro, M., Yamauchi, S., and Fueki, K. (1987). Thermodynamic quantities and defect equilibrium in the perovskite-type oxide solid solution $\text{La}_{1-x}\text{Sr}_x\text{FeO}_{3-\delta}$. *J. Solid State Chem.* 67, 1–8.
22. Park, C.Y., and Jacobson, A.J. (2005). Electrical conductivity and oxygen nonstoichiometry of $\text{La}_{0.2}\text{Sr}_{0.8}\text{Fe}_{0.55}\text{Ti}_{0.45}\text{O}_{3-\delta}$. *J. Electrochem. Soc.* 152, J65.
23. Merkulov, O.V., Markov, A.A., Leonidov, I.A., Patrakeev, M.V., and Kozhevnikov, V.L. (2018). Oxygen nonstoichiometry and thermodynamic quantities in solid solution $\text{SrFe}_{1-x}\text{Sn}_x\text{O}_{3-\delta}$. *J. Solid State Chem.* 262, 121–126.
24. Yuan, W., Ma, Q., Liang, Y., Sun, C., Narayanachari, K.V.L.V., Bedzyk, M.J., Takeuchi, I., and Haile, S.M. (2020). Unexpected trends in the enhanced Ce^{3+} surface concentration in ceria-zirconia catalyst materials. *J. Mater. Chem. A* 8, 9850–9858.
25. McDaniel, A.H., Miller, E.C., Arifin, D., Ambrosini, A., Coker, E.N., O'Hayre, R., Chueh, W.C., and Tong, J. (2013). Sr- and Mn-doped $\text{LaAlO}_{3-\delta}$ for solar thermochemical H_2 and CO production. *Energy Environ. Sci.* 6, 2424–2428.
26. McDaniel, A.H. (2017). Renewable energy carriers derived from concentrating solar power and nonstoichiometric oxides. *Curr. Opin. Green Sustain. Chem.* 4, 37–43.
27. Carrillo, R.J., Warren, K.J., and Scheffe, J.R. (2019). Experimental framework for evaluation of the thermodynamic and kinetic parameters of metal-oxides for solar thermochemical fuel production. *J. Sol. Energy Eng.* 141, 021007.
28. Davenport, T.C., Kemei, M., Ignatowich, M.J., and Haile, S.M. (2017). Interplay of material thermodynamics and surface reaction rate on the kinetics of thermochemical hydrogen production. *Int. J. Hydrogen Energy* 42, 16932–16945.
29. Davenport, T.C., Yang, C.-K., Kucharczyk, C.J., Ignatowich, M.J., and Haile, S.M. (2016). Maximizing fuel production rates in isothermal solar thermochemical fuel production. *Appl. Energy* 183, 1098–1111.
30. Zhao, Z., Uddi, M., Tsvetkov, N., Yildiz, B., and Ghoniem, A.F. (2016). Redox kinetics study of fuel reduced ceria for chemical-looping water splitting. *J. Phys. Chem. C* 120, 16271–16289.
31. Ji, H.-I., Davenport, T.C., Ignatowich, M.J., and Haile, S.M. (2017). Gas-phase vs. material-kinetic limits on the redox response of nonstoichiometric oxides. *Phys. Chem. Chem. Phys.* 19, 7420–7430.
32. Chueh, W.C., and Haile, S.M. (2010). A thermochemical study of ceria: exploiting an old material for new modes of energy conversion and CO_2 mitigation. *Philos. Trans. R. Soc. A* 368, 3269–3294.
33. Yang, C.-K., Yamazaki, Y., Aydin, A., and Haile, S.M. (2014). Thermodynamic and kinetic assessments of strontium-doped lanthanum manganite perovskites for two-step thermochemical water splitting. *J. Mater. Chem. A* 2, 13612–13623.
34. Barcellos, D.R., Sanders, M.D., Tong, J., McDaniel, A.H., and O'Hayre, R.P. (2018). $\text{BaCe}_{0.25}\text{Mn}_{0.75}\text{O}_{3-\delta}$ —a promising perovskite-type oxide for solar thermochemical hydrogen production. *Energy Environ. Sci.* 11, 3256–3265.
35. Zhai, S., Rojas, J., Ahlborg, N., Lim, K., Toney, M.F., Jin, H., Chueh, W.C., and Majumdar, A. (2018). The use of poly-cation oxides to lower the temperature of two-step thermochemical water splitting. *Energy Environ. Sci.* 11, 2172–2178.
36. Chen, Z., Jiang, Q., Cheng, F., Tong, J., Yang, M., Jiang, Z., and Li, C. (2019). Sr- and Co-doped $\text{LaGaO}_{3-\delta}$ with high O_2 and H_2 yields in solar thermochemical water splitting. *J. Mater. Chem. A* 7, 6099–6112.
37. Wang, L., Al-Mamun, M., Liu, P., Wang, Y., Yang, H., and Zhao, H. (2017). $\text{La}_{1-x}\text{Ca}_x\text{Mn}_{1-y}\text{Al}_y\text{O}_3$ perovskites as efficient catalysts for two-step thermochemical water splitting in conjunction with exceptional hydrogen yields. *Chin. J. Catal.* 38, 1079–1086.